

SMARCB1-mediated SWI/SNF complex function is essential for enhancer regulation

Xiaofeng Wang^{1-3,13}, Ryan S Lee^{1-3,13}, Burak H Alver^{4,13}, Jeffrey R Haswell¹⁻³, Su Wang⁴, Jakub Mieczkowski⁵, Yotam Drier^{6,7}, Shawn M Gillespie^{6,7}, Tenley C Archer⁸, Jennifer N Wu¹⁻³, Evgeni P Tzvetkov¹⁻³, Emma C Troisi¹⁻³, Scott L Pomeroy⁸, Jaclyn A Biegel⁹, Michael Y Tolstorukov⁵, Bradley E Bernstein^{6,7,10,14}, Peter J Park^{4,11,14} & Charles W M Roberts^{1-3,12,14}

SMARCB1 (also known as SNF5, INI1, and BAF47), a core subunit of the SWI/SNF (BAF) chromatin-remodeling complex^{1,2}, is inactivated in nearly all pediatric rhabdoid tumors³⁻⁵. These aggressive cancers are among the most genomically stable⁶⁻⁸, suggesting an epigenetic mechanism by which SMARCB1 loss drives transformation. Here we show that, despite having indistinguishable mutational landscapes, human rhabdoid tumors exhibit distinct enhancer H3K27ac signatures, which identify remnants of differentiation programs. We show that SMARCB1 is required for the integrity of SWI/SNF complexes and that its loss alters enhancer targeting—markedly impairing SWI/SNF binding to typical enhancers, particularly those required for differentiation, while maintaining SWI/SNF binding at super-enhancers. We show that these retained super-enhancers are essential for rhabdoid tumor survival, including some that are shared by all subtypes, such as *SPRY1*, and other lineage-specific super-enhancers, such as *SOX2* in brain-derived rhabdoid tumors. Taken together, our findings identify a new chromatin-based epigenetic mechanism underlying the tumor-suppressive activity of SMARCB1.

Loss of SMARCB1 (also known as SNF5, INI1, and BAF47) is the sole driving genetic event that characterizes rhabdoid tumors, which arise in the brain, kidney, and soft tissues⁵. Given the highly malignant behavior of these tumors, in spite of their remarkably simple genomes, we sought to understand how a mutated chromatin regulator might deregulate transcription to drive oncogenesis. We began by characterizing the chromatin landscape of rhabdoid tumors by examining histone modifications in 12 tissue samples and three cell lines derived

from rhabdoid tumors of different tissues (Supplementary Fig. 1a). Most of these had been exome sequenced and are characterized by very low mutation rates and a high degree of purity⁶. Using ChIP-seq, we profiled genome-wide enrichment of three key histone modifications (trimethylation of histone H3 at lysine 4 (H3K4me3), monomethylation of histone H3 at lysine 4 (H3K4me1), and acetylation of histone H3 at lysine 27 (H3K27ac)) to define *cis*-regulatory promoter and enhancer elements⁹. We identified putative active promoters as transcription start site (TSS)-proximal loci containing H3K27ac and H3K4me3 signal and putative enhancers as TSS-distal loci (>2 kb away from active TSSs) containing H3K27ac but not H3K4me3 signal. In Figure 1a–c, we show the Pearson correlation coefficients for the three histone marks among primary tumors, three rhabdoid cell lines, and normal tissues (adult brain, kidney, and other tissues from the NIH Roadmap Epigenomics Project^{10,11}). In comparison to H3K4me3 levels at promoters, H3K4me1 levels at enhancers showed more variability, although tumors, whether primary or cell lines, showed higher within-group correlation than normal tissues (Fig. 1a,b and Supplementary Fig. 1b,c). Notably, evaluation of H3K27ac levels at enhancers identified distinct profiles for each tumor (Fig. 1c and Supplementary Fig. 1d), although there was moderate correlation among some brain-derived samples and among some kidney-derived samples. The presence of subpopulations among brain or kidney rhabdoid tumors is consistent with recent findings based on gene expression and DNA methylation^{12,13}. This suggests that, despite their genomes having low mutation rates, rhabdoid tumors contain substantial variation within the chromatin landscape at enhancers.

Given the much greater variation at enhancers relative to promoters, we focused on enhancers and sought to identify potential enhancer target genes and pathways specific to each subpopulation.

¹Department of Pediatric Oncology, Dana-Farber Cancer Institute, Boston, Massachusetts, USA. ²Division of Hematology/Oncology, Boston Children's Hospital, Boston, Massachusetts, USA. ³Department of Pediatrics, Harvard Medical School, Boston, Massachusetts, USA. ⁴Department of Biomedical Informatics, Harvard Medical School, Boston, Massachusetts, USA. ⁵Department of Molecular Biology, Massachusetts General Hospital, Boston, Massachusetts, USA. ⁶Department of Pathology and Center for Cancer Research, Massachusetts General Hospital and Harvard Medical School, Boston, Massachusetts, USA. ⁷Broad Institute of MIT and Harvard, Cambridge, Massachusetts, USA. ⁸Department of Neurology, Boston Children's Hospital, Harvard Medical School, Boston, Massachusetts, USA. ⁹Department of Pathology and Laboratory Medicine, Children's Hospital Los Angeles and Keck School of Medicine at the University of Southern California, Los Angeles, California, USA. ¹⁰Howard Hughes Medical Institute, Chevy Chase, Maryland, USA. ¹¹Division of Genetics, Brigham and Women's Hospital, Boston, Massachusetts, USA. ¹²Comprehensive Cancer Center and Department of Oncology, St. Jude Children's Research Hospital, Memphis, Tennessee, USA. ¹³These authors contributed equally to this work. ¹⁴These authors jointly directed this work. Correspondence should be addressed to C.W.M.R. (charles.roberts@stjude.org), P.J.P. (peter_park@hms.harvard.edu) or B.E.B. (bernstein.bradley@mgh.harvard.edu).

Received 25 July; accepted 18 November; published online 12 December 2016; doi:10.1038/ng.3746

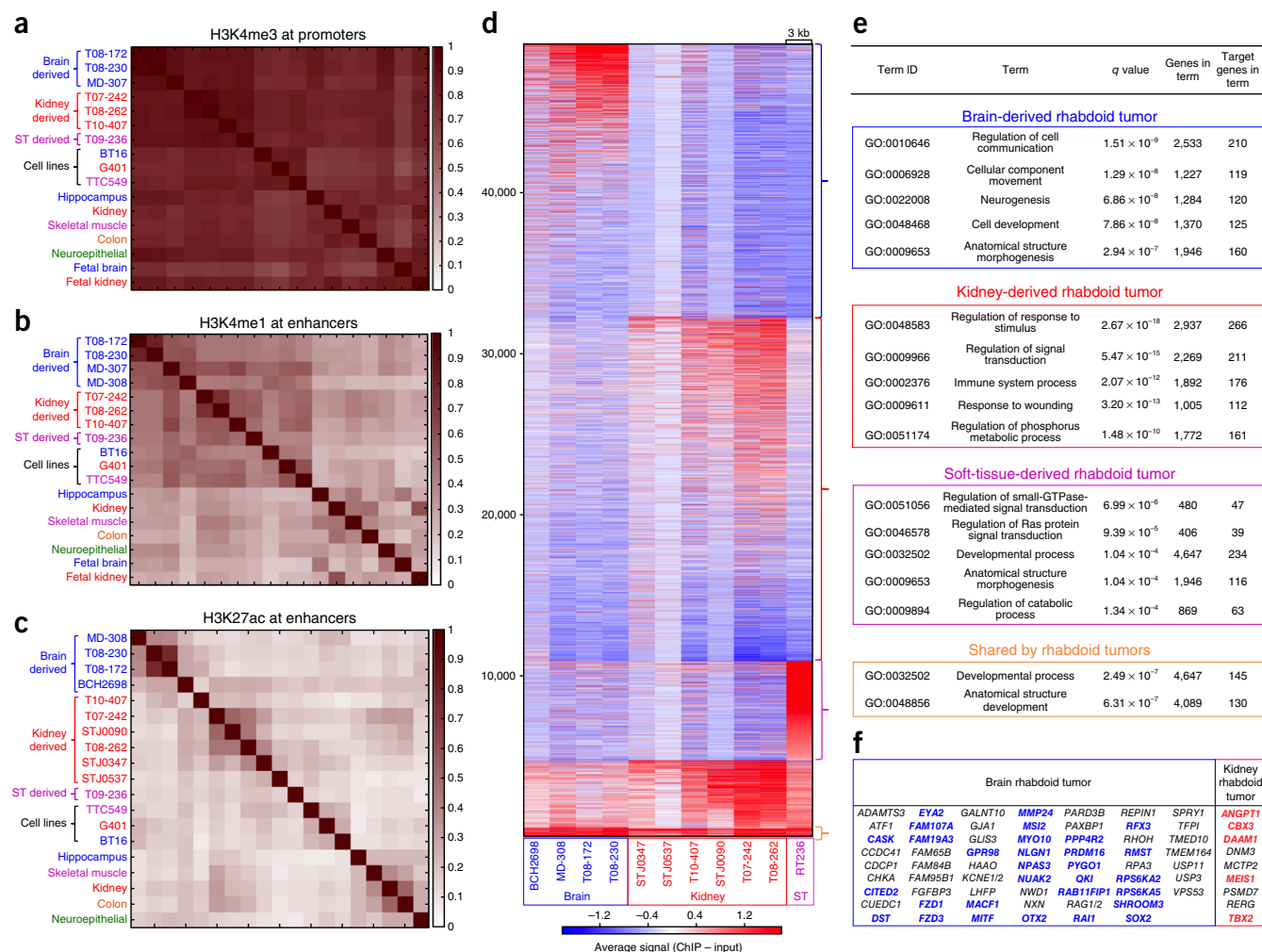


Figure 1 Histone modification landscape in primary rhabdoid tumors and cell lines. Rhabdoid tumors from different tissues show commonalities in H3K4me1 and H3K4me3 signal but are clearly distinct in terms of H3K27ac signal at enhancers. **(a)** Pearson correlations of H3K4me3 signal at the union of all promoters. **(b)** Pearson correlations of H3K4me1 signal at the union of all enhancers. **(c)** Pearson correlations of H3K27ac signal at the union of all enhancers. ST, soft tissue. **(d)** *k*-means clustering of H3K27ac signal at loci called as enhancers. Brain-derived rhabdoid tumor (blue), kidney-derived rhabdoid tumor (red), and soft-tissue-derived rhabdoid tumor (purple) all had enhancers unique to each respective tissue. The orange bracket highlights enhancers shared across all rhabdoid tumors. **(e)** Selected terms from GO analyses of the nearest genes to the top 2,000 enhancers found in each cluster in **d**. A full list of top GO terms appears in **Supplementary Table 1**. **(f)** Super-enhancer-associated genes common across and specific to brain or kidney rhabdoid tumors. The symbols for genes putatively involved in the developmental processes of these respective tissues are bolded and in color.

k-means clustering based on H3K27ac signal at enhancer peaks identified clusters characteristic of rhabdoid tumors from each of the different tissues of origin, as well as a cluster of shared enhancers (Fig. 1d). To analyze the potential role of these enhancer clusters, each enhancer was assigned to the nearest TSS within the same conserved CTCF regulatory boundaries¹⁴. Gene Ontology (GO) analysis performed on the different clusters showed that brain-derived rhabdoid tumors were enriched for active enhancers near neurogenesis-related genes (Fig. 1e and **Supplementary Table 1**), whereas kidney-derived rhabdoid tumors were enriched for terms such as wound healing—a proliferative process thought to involve mesenchymal stem cells¹⁵. A few enhancers were shared by all samples and were enriched for genes associated with developmental processes. Collectively, these findings demonstrate that many enhancers found in rhabdoid tumors are associated with development and that lineage-specific enhancers are present in rhabdoid tumors from different tissues.

Super-enhancers—large clusters of enhancers with high cumulative H3K27ac levels^{16,17}—have recently been implicated as controlling

genes central to maintaining cell identity and, in cancer, genes underlying the malignant state^{16,17}. Using H3K27ac signal to identify super-enhancers, we found a mean of 565 super-enhancers (s.d. = 123) per primary sample and associated these super-enhancers with genes using the same method as above. We found that super-enhancers specific to brain-derived tumors were near key regulators of neural development, such as *SOX2* (ref. 18), *FZD1* and *FZD3* (ref. 19), and others (Fig. 1f and **Supplementary Table 2**). Kidney-derived tumors contained fewer super-enhancers that were specific to the kidney-derived samples but included a super-enhancer proximal to *TBX2*, a regulator of development of the kidney and other organs²⁰. As with all enhancers, these super-enhancers suggest that the persisting shadow of lineage specificity can still be found.

Because the greatest differences seen in the primary tissues were at putative enhancers, we next evaluated whether the loss of SMARCB1 directly contributes to these different TSS-distal H3K27ac signatures. As we previously demonstrated the dependence of rhabdoid tumors on SMARCA4 (BRG1)²¹, suggesting the existence of an essential

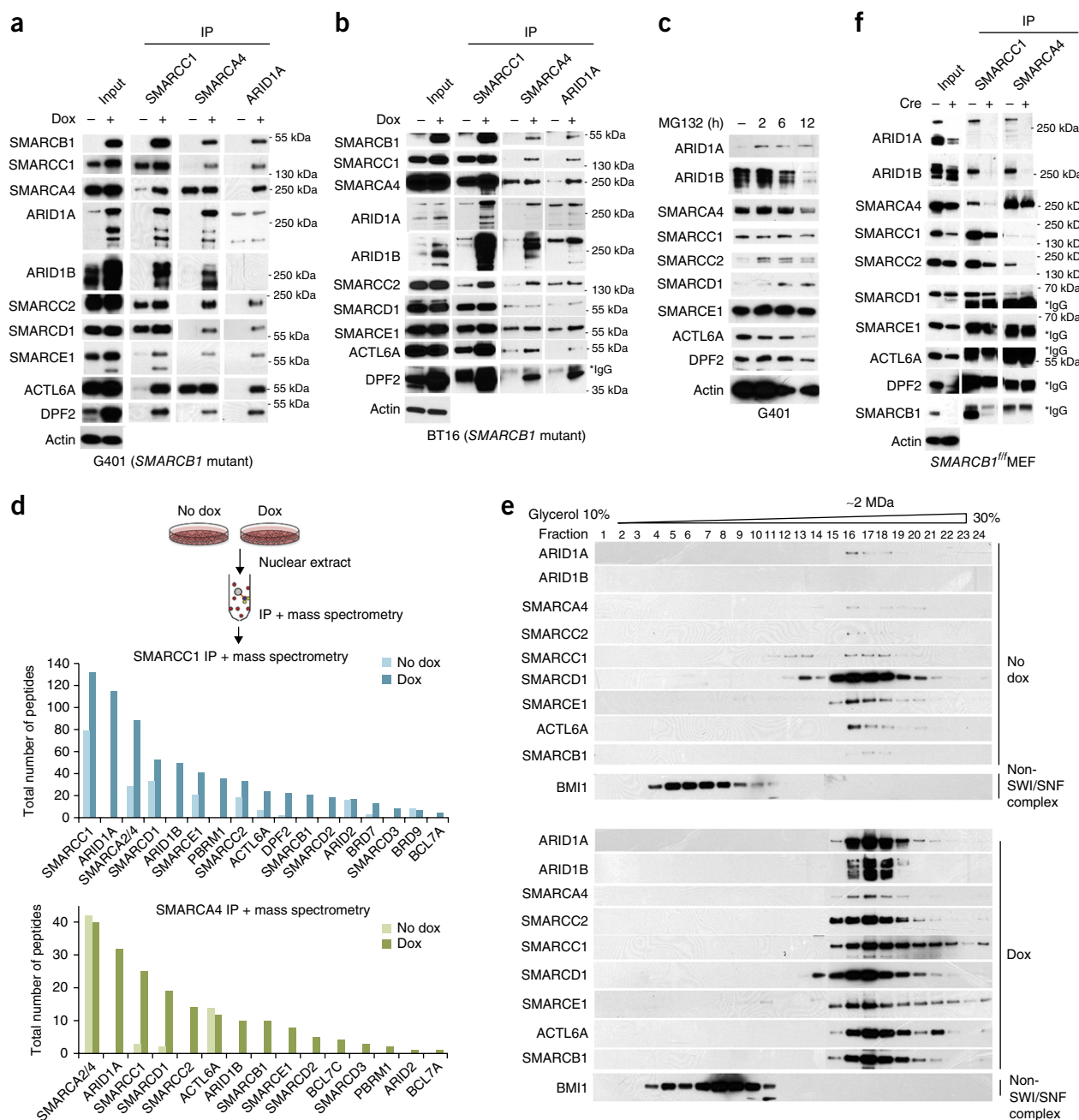


Figure 2 SMARCB1 is essential in maintaining SWI/SNF complex integrity. **(a,b)** Immunoprecipitation (IP) of the SWI/SNF complex subunit SMARCC1, SMARCA4, or ARID1A from nuclear extracts of the G401 **(a)** and BT16 **(b)** cell lines with or without doxycycline (Dox)-induced SMARCB1 re-expression followed by immunoblotting for subunits SMARCB1, SMARCC1, SMARCA4, ARID1A, ARID1B, SMARCC2, SMARCD1, SMARCE1, ACTL6A, and DPF2. Actin is a loading control. **(c)** Protein levels of the indicated SWI/SNF complex subunits upon MG132 treatment in G401 cells. **(d)** Mass spectrometry showing an increased number of peptides from SWI/SNF complex subunits recovered by immunoprecipitation of SMARCA4 and SMARCC1 in G401 cells after SMARCB1 re-expression (doxycycline versus no doxycycline). **(e)** Glycerol (10–30%) sedimentation assay in which the SWI/SNF complex (~2 MDa) was sedimented from *SMARCB1*-deficient G401 cells without (top) or with (bottom) doxycycline followed by immunoblotting for the indicated SWI/SNF complex subunits. BMI1 is a PRC1 complex subunit serving as a control. **(f)** Immunoprecipitation of the SWI/SNF complex by SMARCC1 or SMARCA4 from the nuclear extracts of wild-type or *Smarcb1*-deficient MEFs followed by immunoblotting for the indicated SWI/SNF complex subunits. *Smarcb1* deletion is induced by Cre expression in MEFs. Full blots are provided as **Supplementary Data**.

residual SWI/SNF complex despite the absence of SMARCB1, we sought to evaluate the function of this residual complex on the chromatin landscape. To do so, we established a doxycycline-inducible SMARCB1 expression system.

We first evaluated the contribution of SMARCB1 in forming the SWI/SNF complex. In both the G401 (kidney) and BT16 (brain) rhabdoid

cell lines, SMARCB1 re-expression resulted in drastically increased protein levels for numerous SWI/SNF subunits, particularly the tumor suppressor subunits ARID1A and ARID1B, as well as a marked increase in subunit incorporation into SWI/SNF complexes, as shown by immunoprecipitation of SMARCC1 (BAF155), SMARCA4, and ARID1A (**Fig. 2a,b**). There was no change in the mRNA levels of these subunits

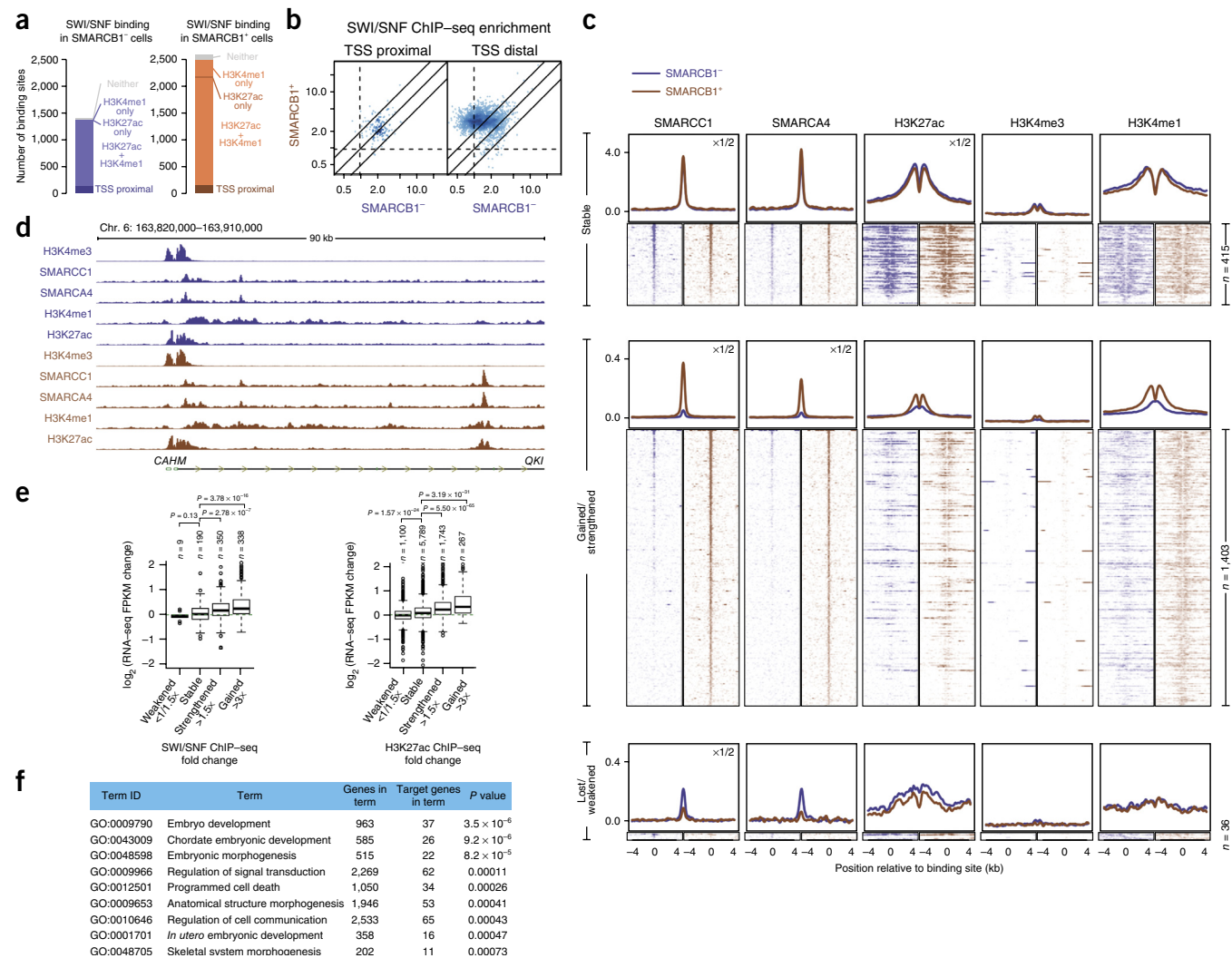


Figure 3 SMARCB1 re-expression alters SWI/SNF complex targeting at typical enhancers. (a) Number of SWI/SNF (SMARCC1 and SMARCA4) binding sites in regions of enrichment for different histone marks in G401 cells with or without SMARCB1 re-expression. (b) Average enrichment of SMARCC1 and SMARCA4 occupancy with versus without SMARCB1 re-expression at TSS-distal or TSS-proximal SWI/SNF binding sites. (c) Heat maps depicting SMARCC1, SMARCA4, H3K27ac, H3K4me1, and H3K4me3 signal intensities for TSS-distal SWI/SNF binding sites, grouped by change upon SMARCB1 re-expression. The rows show 9-kb regions, centered on SMARCC1 and SMARCA4 peaks, ranked by the overall signal intensities of SMARCC1 and SMARCA4. Average profiles for each heat map are shown above, where different y-axis ranges are denoted as 1/2x or 1/4x. (d) Representative screenshot of SMARCC1, SMARCA4, H3K4me1, H3K4me3, and H3K27ac signal with or without SMARCB1 re-expression in G401 cells, showing increased SMARCC1 and SMARCA4 occupancy upon SMARCB1 re-expression accompanied by increased and flanking H3K27ac and H3K4me1 marks at enhancers. (e) Correlation of gene expression changes with SMARCC1 and SMARCA4 binding or H3K27ac signal at TSS-distal binding sites in G401 cells upon addition of doxycycline. For all box plots, the boxes represent 1st, 2nd, and 3rd quartiles, and whiskers show 1.5 times the interquartile range below and above the 1st and 3rd quartiles, respectively. (f) GO analysis of genes proximal to enhancers with increased SMARCC1 and SMARCA4 signal upon addition of doxycycline.

and treatment with MG132 (a proteasome inhibitor) increased the protein levels of some subunits, indicating that the observed changes are the result of post-translational regulation (Fig. 2c and Supplementary Fig. 2a,b). Similar effects were also observed in the TM87 and A204 soft-tissue-derived rhabdoid cell lines (Supplementary Fig. 2c,d). In contrast, induction of exogenous SMARCB1 expression in the control ES2 ovarian cancer cell line with wild-type SMARCB1 had no effect (Supplementary Fig. 2e). Furthermore, immunoprecipitation of SMARCC1 or SMARCA4 followed by mass spectrometry showed that re-expression of SMARCB1 resulted in considerably more peptides corresponding to SWI/SNF subunits (Fig. 2d, Supplementary Fig. 2f, and Supplementary Table 3). To directly evaluate the effect

of SMARCB1 re-expression on SWI/SNF complex integrity, we next performed a glycerol sedimentation assay in G401 and BT16 cells. An intact residual SWI/SNF complex was only faintly detectable before re-expression of SMARCB1 (Fig. 2e and Supplementary Fig. 2g). However, upon re-expression of SMARCB1, we observed markedly increased levels of SWI/SNF complex. Conversely, to evaluate the effect of SMARCB1 loss in normal cells, we used *Smarb1*^{fl/fl} mouse embryonic fibroblasts (MEFs)²². *Smarb1* deletion resulted in substantially reduced protein levels for several SWI/SNF subunits, including ARID1A and ARID1B, and reduced subunit incorporation into the complex without concomitant changes in mRNA levels (Fig. 2f and Supplementary Fig. 2h). These biochemical studies demonstrate that

SMARCB1 is essential for SWI/SNF complex stability, particularly for ARID1A, the most frequently mutated SWI/SNF subunit in cancer.

We next investigated how this alteration in SWI/SNF complex composition and abundance affects complex targeting and binding. We performed ChIP-seq analysis of the core SWI/SNF subunits SMARCA4 and SMARCC1 in the G401, BT16, and TTC549 rhabdoid lines for which we

had also profiled histone marks (Supplementary Fig. 1a), before and after induction of SMARCB1 expression. SMARCB1 expression led to a substantial increase in occupancy by SMARCA4 and SMARCC1, which were themselves highly correlated, with many more binding sites gained than lost (Fig. 3a,b and Supplementary Figs. 3a–c, 4a,b, and 5a,b). Although the role of SWI/SNF complexes in organizing nucleosomes at promoters

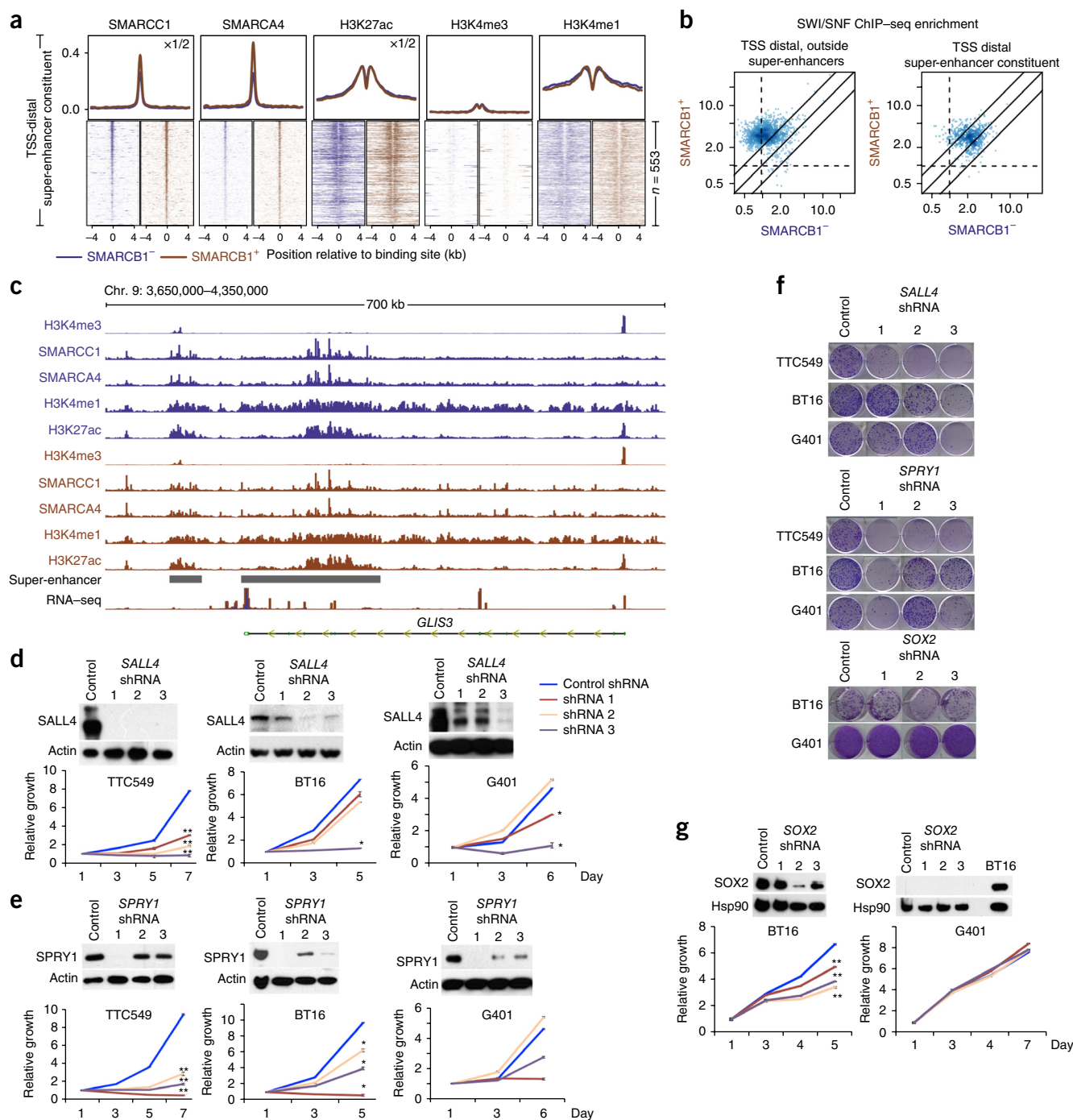


Figure 4 Residual SWI/SNF complexes are specifically maintained at super-enhancers in *SMARCB1*-deficient rhabdoid tumors. (a) Heat maps depicting SMARCC1, SMARCA4, H3K27ac, H3K4me1, and H3K4me3 signal intensities for SMARCC1 and SMARCA4 bound within super-enhancers. (b) Scatterplots showing the change in average SMARCC1 and SMARCA4 signal for TSS-proximal binding sites or TSS-distal binding sites split into those outside and inside super-enhancers. (c) Representative screenshot in G401 cells showing limited changes in SMARCC1, SMARCA4, H3K27ac, or H3K4me1 upon SMARCB1 re-expression inside super-enhancers, in contrast to outside super-enhancers. (d–g) Knockdown of *SALL4* (d) or *SPRY1* (e) in G401, BT16, and TTC549 cells affects cell proliferation and colony-forming ability (d–f), whereas knockdown of *SOX2* (g) affects the proliferation and colony-forming abilities of BT16 but not G401 cells (f,g). Error bars, s.d.; * $P < 0.05$, ** $P < 0.001$ (t test, two-sides; $n = 3$ technical replicates).

has been established²³, we observed that the majority of SWI/SNF binding instead occurred at TSS-distal enhancers marked with H3K4me1 and/or H3K27ac (Fig. 3a and Supplementary Figs. 4a and 5a), consistent with recent reports showing SMARCA4 binding to enhancers^{24–26}. As was the case in the absence of SMARCB1, the majority of SWI/SNF targeting was gained at TSS-distal sites (Fig. 3a,b). Thus, with or without SMARCB1, the SWI/SNF complex is predominantly targeted to TSS-distal sites, with the number of sites markedly increased in the presence of SMARCB1.

To investigate a link between SMARCB1 and enhancer regulation, we categorized TSS-distal SWI/SNF targets on the basis of their sensitivity to SMARCB1 re-expression, defining them as sites that were lost (>1.5-fold reduction), gained (>1.5-fold gain), or unchanged. At sites that were gained, we observed increased enhancer-associated H3K27ac and H3K4me1 signal flanking the peak SWI/SNF binding position (Fig. 3c,d and Supplementary Figs. 4c,d and 5c,d). Conversely, the few sites that were lost showed a decrease in H3K27ac levels. These findings identify SWI/SNF as being preferentially active at enhancers and establish a direct role for SMARCB1 in generating the active chromatin landscape at enhancers.

To investigate the biological relevance of SMARCB1 to enhancer function, we performed RNA-seq analysis on six rhabdoid tumor cell lines, including those described above, before and after SMARCB1 re-expression. There were many more genes upregulated (between 303 and 564 coding genes with >2-fold increase across the six cell lines) than downregulated (between 17 and 86 coding genes with >2-fold decrease across the six cell lines) (Supplementary Fig. 6), and the changes correlated with nearby TSS-distal SWI/SNF binding and enhancer changes (Fig. 3e and Supplementary Figs. 4e and 5e). In contrast to a previous report that SMARCB1 is dispensable for the control of a handful of genes with SMARCA4-dependent expression²⁷, our results demonstrate that SMARCB1 loss affects a large majority of SWI/SNF-regulated genes. To gain insight into the effects of SMARCB1-mediated enhancer induction, we performed GO enrichment analysis for genes near enhancers with increased SWI/SNF binding upon SMARCB1 re-expression, relative to all enhancer-proximal genes (Online Methods). For all three cell types, the identified GO terms were particularly associated with development and differentiation. Cell-type-specific GO terms were also observed, such as morphogenesis of branching epithelium in kidney-derived G401 rhabdoid cells and neuron differentiation in brain-derived BT16 rhabdoid cells (Fig. 3f, Supplementary Figs. 4f and 5f, and Supplementary Table 4). Consistent with a shared mechanistic basis among the different tissue types, however, both GO analysis and gene set enrichment analysis (GSEA) of differentially expressed genes across all the cell lines identified commonly shared terms, including developmental process, cell differentiation, and SMARCB1 targets (Supplementary Figs. 6 and 7). Collectively, these findings demonstrate that SMARCB1 re-expression results in increased SWI/SNF complex enrichment at enhancers, particularly those related to development and differentiation, in gained chromatin marks reflective of an active state, and in upregulated expression of genes associated with tissue-specific differentiation.

Having identified a role for SMARCB1 in the control of enhancer formation and function, we next asked whether SMARCB1 contributes to super-enhancer formation and function. Because of the distinct structure of super-enhancers, the concentration of constituent proteins required to maintain their integrity has been shown to differ substantially from that required to maintain the integrity of regular enhancers²⁸. Unlike the effect upon typical enhancers, we did not observe appreciable changes in the number or position of super-enhancers upon SMARCB1 re-expression (Supplementary Fig. 8a–c). Even without SMARCB1, the SWI/SNF complex was already bound at super-enhancers (Fig. 4a–c and Supplementary Fig. 9a,b). SMARCB1

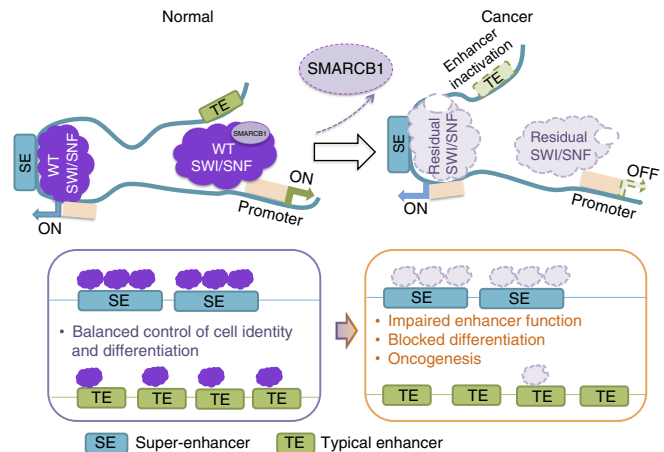


Figure 5 Working model. SMARCB1 functions to stabilize the SWI/SNF complex, thus enabling it to bind and facilitate enhancer formation and function. Loss of SMARCB1 results in markedly reduced levels of the SWI/SNF complex, which results in reduced genome-wide targeting at regular enhancers, thus impairing their functions. However, the small amount of residual SWI/SNF complex preferentially present at super-enhancers is key to maintaining aberrant cell identity.

re-expression facilitated only a modest increase in SWI/SNF binding at super-enhancers, and this increased binding had no effect on the levels of H3K27ac or H3K4me1 (Fig. 4a,b and Supplementary Fig. 9a–d). This observation suggests that SMARCB1 has different functions at regular enhancers in comparison to super-enhancers—it serves a role in the activation of differentiation-related regular enhancers but is largely dispensable for super-enhancers (Fig. 4b,c). We confirmed binding of the residual complex at super-enhancers by performing ChIP–qPCR (Supplementary Fig. 10) and found that further reduction of SWI/SNF levels via knockdown of either *SMARCC1* or *SMARCD1* resulted in reduced residual complex binding at the super-enhancer accompanied by reduced gene expression (Supplementary Fig. 10). The preferential targeting of the residual complex to super-enhancers may be due to a higher density of transcriptional co-regulators at super-enhancers, resulting in higher affinity for and greater stability of the SWI/SNF complex, in comparison to typical enhancers.

Given that the mutational burden is similarly low among rhabdoid tumors from different tissues, we reasoned that super-enhancers shared by rhabdoid tumors from different organs might be associated with genes essential for tumor cell survival. To define this set of shared super-enhancers, we identified those that (i) overlapped with the most commonly shared enhancers found in the bottommost cluster of Figure 1d, (ii) were identified in all three rhabdoid tumor cell lines, and (iii) were not found in normal tissues. Among the ten super-enhancers meeting these criteria were ones proximal to *SPRY1*, *SALL4*, and *HMG2* (Supplementary Fig. 11a–c). Interestingly, *HMG2* has previously been implicated in rhabdoid tumor proliferation²⁹. We found that *SALL4* and *SPRY1* are also essential for rhabdoid tumor proliferation, as short hairpin RNA (shRNA)-mediated knockdown of either of these genes significantly impaired the proliferation of all three cell lines tested (Fig. 4d–f). Meanwhile, as mentioned above, we found that the *SOX2*-associated super-enhancer was specific to brain rhabdoid tumors (Supplementary Fig. 11d), suggesting that tissue-specific super-enhancers could also be essential for the survival of cancer cells. Consistent with this notion, shRNA-mediated knockdown of *SOX2* specifically impaired the proliferation of BT16 cells but had no effect on G401 cells (Fig. 4f,g).

Taken together, our findings present a mechanistic framework for the function of SMARCB1 in the control of cell identity and the mechanism by which mutation of this core SWI/SNF subunit drives cancer formation (Fig. 5): SMARCB1 functions to stabilize the SWI/SNF complex, enabling it to bind and facilitate enhancer formation and function. SMARCB1 loss results in a marked reduction in the amount of SWI/SNF complexes, decreasing their levels such that they are unable to maintain normal enhancer function. The small amount of residual SWI/SNF complex that remains is preferentially bound to super-enhancers. It is notable that, whereas activation of regular enhancers is essential for differentiation, super-enhancers have been implicated in the maintenance of current cell identity. It is of further note that, despite the extremely rapid onset of cancer caused by *Smrbc1* inactivation in mice, only extremely specific cell types are susceptible to transformation³⁰, whereas the vast majority of cell types undergo arrest following SMARCB1 loss. Similarly, the spectrum of cancers associated with SMARCB1 loss in humans is quite specific. These findings collectively suggest a model in which loss of SMARCB1 impairs the function of enhancers that are required for differentiation, whereas super-enhancers that underlie the current cell state are largely unaffected. In specific proliferative progenitor cell types, then, the consequence of reduced enhancer function with super-enhancer preservation may be to drive oncogenic transformation by locking cells into a poorly differentiated and highly proliferative state. Collectively, our work provides key insights into the mechanisms by which SWI/SNF subunit mutations cause cancer through impairment of enhancer function and supports super-enhancer-specified genes as essential in these cancers, thus identifying potential therapeutic targets.

METHODS

Methods, including statements of data availability and any associated accession codes and references, are available in the [online version of the paper](#).

Accession codes. All sequencing data have been submitted to the Gene Expression Omnibus (GEO) under accession [GSE71506](#).

Note: Any Supplementary Information and Source Data files are available in the online version of the paper.

ACKNOWLEDGMENTS

We thank members of the Roberts and Park laboratories for assistance and discussion. We thank J. Francois (Boston Children's Hospital), J. Roth (Children's Hospital of Philadelphia), M. Lear (St. Jude Children's Research Hospital), and J. Silterra (Broad Institute) for their help in acquiring and performing preliminary clinical analysis of primary tumor samples; R. Rubio (Dana-Farber Cancer Institute) and M. Uziel (Broad Institute) for their assistance in sequencing samples; N. Shores (Broad Institute) for assistance in accessing Roadmap Epigenomics data; and R. Tomaino (Harvard Medical School) for assistance in proteomic analysis. X.W. was supported by the Pathway to Independence Award from the US National Institutes of Health (K99CA197640), a postdoctoral fellowship from the Rally Foundation for Childhood Cancer Research and The Truth 365, and a research grant from St. Baldrick's Foundation. R.S.L. was partially supported by an NSF Graduate Research Fellowship. This work was supported by US National Institutes of Health grants R01CA172152 (C.W.M.R.), R01CA113794 (C.W.M.R.), and U54HG006991 (B.E.B.). The Avalanna Fund, the Cure AT/RT Now Foundation, the Garrett B. Smith Foundation, Miles for Mary, and ALSAC/St. Jude (C.W.M.R.) provided additional support.

AUTHOR CONTRIBUTIONS

X.W., R.S.L., B.H.A., B.E.B., P.J.P., and C.W.M.R. conceived the experiments and study design. X.W., J.R.H., E.P.T., and E.C.T. performed all cell line experiments. R.S.L. and S.M.G. performed all primary tumor experiments. B.H.A., R.S.L., S.W., J.M., and Y.D. performed computational analyses of the data. X.W., R.S.L., B.H.A., and S.W. performed statistical analyses. T.C.A., S.L.P., and J.A.B. contributed primary tumor samples and clinical data. J.N.W. designed the SMARCB1

re-expression vector. X.W., R.S.L., B.H.A., J.R.H., J.M., Y.D., M.Y.T., B.E.B., P.J.P., and C.W.M.R. contributed to the interpretation of experiments. X.W., R.S.L., B.H.A., and C.W.M.R. wrote the manuscript with input from all co-authors.

COMPETING FINANCIAL INTERESTS

The authors declare no competing financial interests.

Reprints and permissions information is available online at <http://www.nature.com/reprints/index.html>.

- Wilson, B.G. & Roberts, C.W.M. SWI/SNF nucleosome remodellers and cancer. *Nat. Rev. Cancer* **11**, 481–492 (2011).
- Wu, J.I., Lessard, J. & Crabtree, G.R. Understanding the words of chromatin regulation. *Cell* **136**, 200–206 (2009).
- Biegel, J.A. *et al.* Germ-line and acquired mutations of *IN1* in atypical teratoid and rhabdoid tumors. *Cancer Res.* **59**, 74–79 (1999).
- Versteeg, I. *et al.* Truncating mutations of *hSNF5/IN1* in aggressive paediatric cancer. *Nature* **394**, 203–206 (1998).
- Eaton, K.W., Tooke, L.S., Wainwright, L.M., Judkins, A.R. & Biegel, J.A. Spectrum of *SMARCB1/IN1* mutations in familial and sporadic rhabdoid tumors. *Pediatr. Blood Cancer* **56**, 7–15 (2011).
- Lee, R.S. *et al.* A remarkably simple genome underlies highly malignant pediatric rhabdoid cancers. *J. Clin. Invest.* **122**, 2983–2988 (2012).
- Hasselblatt, M. *et al.* High-resolution genomic analysis suggests the absence of recurrent genomic alterations other than *SMARCB1* aberrations in atypical teratoid/rhabdoid tumors. *Genes Chromosom. Cancer* **52**, 185–190 (2013).
- Lawrence, M.S. *et al.* Mutational heterogeneity in cancer and the search for new cancer-associated genes. *Nature* **499**, 214–218 (2013).
- Zhou, V.W., Goren, A. & Bernstein, B.E. Charting histone modifications and the functional organization of mammalian genomes. *Nat. Rev. Genet.* **12**, 7–18 (2011).
- Zhu, J. *et al.* Genome-wide chromatin state transitions associated with developmental and environmental cues. *Cell* **152**, 642–654 (2013).
- Roadmap Epigenomics Consortium. *et al.* Integrative analysis of 111 reference human epigenomes. *Nature* **518**, 317–330 (2015).
- Chun, H.-J.E. *et al.* Genome-wide profiles of extra-cranial malignant rhabdoid tumors reveal heterogeneity and dysregulated developmental pathways. *Cancer Cell* **29**, 394–406 (2016).
- Johann, P.D. *et al.* Atypical teratoid/rhabdoid tumors are comprised of three epigenetic subgroups with distinct enhancer landscapes. *Cancer Cell* **29**, 379–393 (2016).
- Wang, S. *et al.* Target analysis by integration of transcriptome and ChIP-seq data with BETA. *Nat. Protoc.* **8**, 2502–2515 (2013).
- Stappenbeck, T.S. & Miyoshi, H. The role of stromal stem cells in tissue regeneration and wound repair. *Science* **324**, 1666–1669 (2009).
- Whyte, W.A. *et al.* Master transcription factors and Mediator establish super-enhancers at key cell identity genes. *Cell* **153**, 307–319 (2013).
- Hnisz, D. *et al.* Super-enhancers in the control of cell identity and disease. *Cell* **155**, 934–947 (2013).
- Bergsland, M. *et al.* Sequentially acting Sox transcription factors in neural lineage development. *Genes Dev.* **25**, 2453–2464 (2011).
- Yu, H. *et al.* Frizzled 1 and frizzled 2 genes function in palate, ventricular septum and neural tube closure: general implications for tissue fusion processes. *Development* **137**, 3707–3717 (2010).
- Abrahams, A., Parker, M.I. & Prince, S. The T-box transcription factor Tbx2: its role in development and possible implication in cancer. *IUBMB Life* **62**, 92–102 (2010).
- Wang, X. *et al.* Oncogenesis caused by loss of the SNF5 tumor suppressor is dependent on activity of BRG1, the ATPase of the SWI/SNF chromatin remodeling complex. *Cancer Res.* **69**, 8094–8101 (2009).
- Isakoff, M.S. *et al.* Inactivation of the Snf5 tumor suppressor stimulates cell cycle progression and cooperates with p53 loss in oncogenic transformation. *Proc. Natl. Acad. Sci. USA* **102**, 17745–17750 (2005).
- Tolstorukov, M.Y. *et al.* Swi/Snf chromatin remodeling/tumor suppressor complex establishes nucleosome occupancy at target promoters. *Proc. Natl. Acad. Sci. USA* **110**, 10165–10170 (2013).
- Yu, Y. *et al.* Olig2 targets chromatin remodelers to enhancers to initiate oligodendrocyte differentiation. *Cell* **152**, 248–261 (2013).
- Bossen, C. *et al.* The chromatin remodeler Brg1 activates enhancer repertoires to establish B cell identity and modulate cell growth. *Nat. Immunol.* **16**, 775–784 (2015).
- Alexander, J.M. *et al.* Brg1 modulates enhancer activation in mesoderm lineage commitment. *Development* **142**, 1418–1430 (2015).
- Doan, D.N. *et al.* Loss of the IN1 tumor suppressor does not impair the expression of multiple BRG1-dependent genes or the assembly of SWI/SNF enzymes. *Oncogene* **23**, 3462–3473 (2004).
- Lövén, J. *et al.* Selective inhibition of tumor oncogenes by disruption of super-enhancers. *Cell* **153**, 320–334 (2013).
- Kaur, H. *et al.* The chromatin-modifying protein HMG2 promotes atypical teratoid/rhabdoid cell tumorigenicity. *J. Neuropathol. Exp. Neurol.* **74**, 177–185 (2015).
- Wang, X. *et al.* TCR-dependent transformation of mature memory phenotype T cells in mice. *J. Clin. Invest.* **121**, 3834–3845 (2011).

ONLINE METHODS

Human primary tumor samples. Primary human tumor samples were collected and flash frozen. Tumors were reviewed to confirm the diagnosis and to estimate tumor content (Children's Hospital of Philadelphia and Boston Children's Hospital). All tumors have previously been exome sequenced⁵. Patients' guardians provided informed consent before their participation. Local institutional review boards (Children's Hospital of Philadelphia and Boston Children's Hospital) approved the collection and testing of each sample. Tissue was mechanically macerated while frozen and suspended in PBS with protease inhibitor.

Cell culture. The G401, G402, A204, and ES-2 cell lines were purchased from the American Type Culture Collection. BT12, BT16, TM87-16, and TTC549 cells were maintained in the laboratory. All cells have been tested negative for mycoplasma contamination. G401 and BT16 cells were cultured in DMEM with 10% FBS, G402, TM87-16, and ES-2 cells were cultured in McCoy's with 10% FBS, TTC549 cells were cultured in RPMI with 10% FBS, and BT12 cells were cultured in Opti-MEM (Life Technologies) with 5% FBS, at 37 °C with 5% CO₂. MEFs were generated as described previously³¹. To establish stable cell lines with inducible re-expression of SMARCB1, cells were transduced with lentivirus pInducer-21-SMARCB1. At 72 h after transduction, GFP-positive cells were sorted and maintained in medium with Tet-System Approved FBS (Clontech, 631106). To induce SMARCB1 re-expression, cells were treated with doxycycline (1 µg/ml; EMD Millipore) for the indicated time. For shRNA-mediated knockdown, cells were transduced with lentiviral shRNAs and selected with puromycin for 72 h before seeding for MTT or colony formation assays. MTT assays were conducted with an MTT Cell Proliferation kit (Roche Diagnostics, 11465007001). Colony formation assays were conducted by staining cells for 20 min with crystal violet staining solution (0.05% crystal violet, 1% formaldehyde, 1% PBS, and 1% methanol).

shRNAs to *SALL4* (TRCN0000433893, TRCN0000419286, and TRCN000021874) and *SPRY1* (TRCN0000344734, TRCN0000369465, and TRCN0000344733) were obtained from the RNA interference (RNAi) screening core facility at the Dana-Farber Cancer Institute and shRNAs to *SOX2* were purchased from GE Healthcare (V2LHS_153337, V3LHS_404430, and V3LHS_404432). shRNA constructs were lentivirally transduced into G401, TTC549, and BT16 cells. Non-silencing control shRNA was in the pLKO.1 lentiviral expression vector backbone³¹.

Coimmunoprecipitation and mass spectrometry. Nuclear extracts for coimmunoprecipitation were prepared using the NE-PER Nuclear and Cytoplasmic Extraction kit (Thermo Scientific, 78835). Nuclear extracts were diluted with RIPA buffer (150 mM NaCl, 50 mM Tris-HCl pH 7.5, 1% Nonidet P-40, 0.5% sodium deoxycholate, 0.1% SDS, and 1 mM DTT) to a final concentration of 1 mg/ml (with protease inhibitor cocktail, Roche). Each immunoprecipitation was incubated with antibody overnight at 4 °C. Protein G Dynabeads (Life Technologies, 10009D) were added, and samples were incubated at 4 °C for 3 h. Beads were then washed three times with RIPA buffer and resuspended in reducing SDS gel loading buffer. Antibodies to the following proteins were used in the immunoprecipitation and immunoblots: SMARCC1 (BAF155; Santa Cruz Biotechnology, sc-9746, 1:1,000 dilution), ARID1A (Santa Cruz Biotechnology, sc-32761 for immunoprecipitation, 2 µg/mg lysate; Cell Signaling Technology, 12354 for immunoblotting, 1:1,000 dilution), ARID1B (Abcam, ab54761, 1:1,000 dilution), SMARCA4 (BRG1; Santa Cruz Biotechnology, sc-17796, 1:300 dilution), SMARCC2 (BAF170; Bethyl Laboratories, A301-039A, 1:1,000 dilution), SMARCD1 (BAF60A; Bethyl Laboratories, A301-595A, 1:3,000 dilution), SMARCE1 (BAF57; Bethyl Laboratories, A300-810A, 1:3,000 dilution), SMARCB1 (SNF5; Bethyl Laboratories, A301-087A, 1:5,000 dilution), ACTL6A (BAF53A; Bethyl Laboratories, A301-391A, 1:3,000 dilution), and actin (Cell Signaling Technology, 5125, 1:1,000 dilution).

For mass spectrometry, equal amounts of nuclear extract were used for each immunoprecipitation. Samples after immunoprecipitation were separated on a NUPAGE 12% Bis-Tris gel and stained with SimplyBlue SafeStain (Life Technologies). For each immunoprecipitation sample, the whole lane was cut and sent for protein identification at the Taplin Mass Spectrometry Facility of Harvard Medical School.

Glycerol sedimentation assays. Nuclear fractions for sedimentation assays were prepared according to previous literature³². Briefly, cells were collected at the indicated time points and then lysed and homogenized in Buffer A (10 mM HEPES pH 7.6, 25 mM KCl, 1 mM EDTA, 10% glycerol, 1 mM DTT, and protease inhibitors (Complete tablets, Roche) supplemented with 1 mM PMSF) on ice. Nuclei were sedimented by centrifugation (1,000g for 10 min), resuspended in Buffer B (10 mM HEPES pH 7.6, 3 mM MgCl₂, 100 mM KCl, 0.1 mM EDTA, 10% glycerol, 1 mM DTT, and protease inhibitors) and further lysed by the addition of ammonium sulfate to a final concentration of 0.3 M. Soluble nuclear proteins were separated from the insoluble chromatin fraction by ultracentrifugation (100,000g for 20 min) and precipitated with 0.3 mg/ml ammonium sulfate for 20 min on ice. Protein precipitate was isolated by ultracentrifugation (100,000g for 30 min) and resuspended in Buffer A without glycerol. Then, 1 mg of nuclear extract was carefully overlaid onto a 12-ml 10–30% glycerol gradient (in RIPA buffer) prepared in a 14-ml 14 × 95 mm polyallomer centrifuge tube (Beckman Coulter, 331374). Tubes were placed in an SW-40 Ti swing-bucket rotor and centrifuged at 4 °C for 16 h at 40,000 r.p.m. Fractions (0.5 ml) were collected and used in gel electrophoresis and subsequent immunoblotting analyses. Immunoblots of complex subunits were developed on the same film with the same exposure times for the no-doxycycline and doxycycline samples for proper comparison.

ChIP-seq and RNA-seq. Primary tissue was singly cross-linked using 1% formaldehyde for 10 min, and cross-linking was quenched with 2.5 M glycine for 5 min. Dual cross-linking was used for ChIP-seq analysis of SWI/SNF complex subunits in cancer cell lines. Briefly, cells were first cross-linked in 2 mM disuccinimidyl glutarate (DSG; Life Technologies, 20593) for 30 min and then cross-linked in 1% formaldehyde for 10 min, with reactions quenched with glycine for 5 min. Cells were washed with PBS three times and then used to generate nuclear extract. Chromatin was fragmented using sonication (Branson sonifier with microtip) for primary tissues or the adaptive focused acoustics (AFA) technology developed by Covaris for cell lines. Solubilized chromatin was immunoprecipitated with antibodies against SMARCA4 (BRG1; Abcam, ab110641, 10 µl), SMARCC1 (BAF155; Santa Cruz Biotechnology, sc-9746, 10 µg), H3K4me1 (Abcam, ab8895, 5 µg), H3K4me3 (Millipore, 07-473, 5 µl), and H3K27ac (Cell Signaling Technology, 8173, 5 µl). Antibody–chromatin complexes were pulled down with Protein G Dynabeads (Life Technologies), washed, and then eluted. After cross-linking reversal and treatment with RNase A and proteinase K, ChIP DNA was extracted with the MinElute PCR purification kit (Qiagen). ChIP DNA was quantified with the Quant-it PicoGreen dsDNA Assay kit (Life Technologies). 10 ng of ChIP DNA per sample was used to prepare sequencing libraries, and ChIP DNA and input controls were sequenced with the Illumina HiSeq Genome Analyzer.

For RNA-seq, total RNA was extracted using TRIzol Reagent (Invitrogen) and further purified using the RNeasy MinElute Cleanup kit (Qiagen). 2 µg of total RNA was used to generate each RNA-seq library using the TruSeq Total RNA Sample Prep kit (Illumina), and libraries were sequenced with the Illumina HiSeq Genome Analyzer.

ChIP-seq processing. Alignment, fragment size estimation, and library complexity. Sequenced reads were aligned to the hg19 genome assembly using Bowtie 0.12.6 (ref. 33), allowing up to ten matches ('-m 10--best' options). Reads on the 24 assembled chromosomes excluding the ENCODE blacklisted regions were kept for downstream analysis. Peaks of cross-correlation profiles were identified to estimate the typical fragment size for each sample. The typical fragment size for the different samples ranged from 140–180 bp. Each read was considered to represent a signal at half the typical fragment size from the 5' end. Library complexity was calculated for each sample as the number of unique base-pair positions mapped on each strand divided by the number of reads. For batches of experiments where the typical library complexity was below 80% (RT172, RT230, RT307, RT308, and RT407), only one read mapping to each position was kept.

Identification of regions of enrichment. Regions of enrichment (RoEs) of H3K27ac, SMARCC1, and SMARCA4 in ChIP-seq were called using the SPP package³⁴ in R, with the function `get.broad.enrichment.clusters` and options `window.size = 500` and `z.thr = 4`, using matching input data for each sample. For H3K4me3 tracks that showed a clearer signal at promoters, the same

approach was taken with $z_{thr} = 5$. Overlapping SMARCA4 and SMARCC1 RoEs with $z_{thr} = 4$ were used as SWI/SNF binding sites. Finally, the union of calls from the no-doxycycline and doxycycline conditions was calculated for each cell line. The last step reduces any bias that may arise in differential RoE calling from thresholds. Sequencing of two input samples (RT307 and RT308) failed because of a limited amount of available material from primary tissues. The input sample for RT230, which is also a brain rhabdoid tumor, was used for RoE calling in RT307 and RT308.

Classification of regions of enrichment on the basis of position relative to TSSs. Active TSSs were defined in a cell type as all TSSs defined in Ensembl release GRCh37.72 that overlapped an H3K4me3 peak. H3K27ac or SWI/SNF RoEs that overlapped both an H3K4me3 RoE and an active TSS were called as TSS-proximal sites. Those more than 1 kb away from an H3K4me3 RoE and more than 2 kb away from an active TSS were called as TSS-distal sites. The TSS-proximal H3K27ac RoEs are referred to as active promoters, and the TSS-distal ones are referred to as active enhancers.

Sequencing of the H3K4me3 sample failed for RT308. Active TSSs for this sample were called on the basis of the presence of strong (SPP broad enrichment call with $z_{thr} = 5$) H3K27ac RoEs overlapping Ensembl TSSs. Where H3K4me3 RoE calls were required in downstream analyses (TSS-distal/TSS-proximal calls, suprt-enhancer calling), the union of H3K4me3 RoEs for the other primary rhabdoid tumor samples was substituted.

Correlation and principal-component analyses of primary rhabdoid tumor samples. The correlation analysis and principal-component analysis presented in **Figure 1** and **Supplementary Figure 1** were conducted using MATLAB. For H3K4me1 and H3K27ac, the read-count-normalized immunoprecipitation signal for respective modifications was calculated for each enhancer from the union of all enhancers found across the represented tissues. Similarly, for H3K4me3, the read-count-normalized immunoprecipitation signal was calculated for each promoter from the union of all promoters identified across all the represented tissues. Pearson linear correlation coefficients were calculated using the `corrcoef` function, and principal-component analysis used the `pca` function.

Clustering of primary rhabdoid tumor sample enhancers. For the heat map in **Figure 1d**, Cluster 3.0 (ref. 35) was used to perform k -means clustering with a Euclidean distance metric and Java TreeView³⁶ was used for visualization. The H3K27ac signal in the heat map represents the immunoprecipitation signal minus input for a $\pm 1,500$ -bp window centered on the peak signal for each enhancer. Clusters of enhancers specific to brain-, kidney-, and soft-tissue-derived rhabdoid tumors were then combined for GO analysis.

Immunoprecipitation efficiency correction for H3K27ac samples. The efficiency of immunoprecipitation may vary in different ChIP-seq experiments. A number of lines of evidence suggested that real levels of H3K27ac are unchanged at a large proportion of promoters upon SMARCB1 re-expression: (i) we found that a large portion of promoters showed the same amount of fold change with very small variance; (ii) the typical fold change was independent of SWI/SNF binding at promoters and was the same as at enhancers with no SWI/SNF binding; and (iii) in an accompanying study with MEFs, we observed different average fold change trends at promoters, both greater than and close to one-fold for replicates of experiments upon *Smarb1* knockout, whereas we saw consistent decrease of H3K27ac levels in immunoblots, and at enhancers. On the basis of these observations, we applied a small multiplicative factor to H3K27ac samples to set the mode of the log-transformed fold change distribution at promoters to zero while comparing doxycycline and no-doxycycline samples. These factors were as follows: G401: no doxycycline, 1.15; doxycycline, 0.86; BT16: no doxycycline, 1.11; doxycycline, 0.9; TTC549: no doxycycline, 1.00; doxycycline, 1.00. This normalization procedure does not affect the qualitative observations presented. We refrained from applying similar normalization for other ChIP-seq sample pairs because we could not confidently determine a set of regions where they were unaffected upon SMARCB1 re-expression.

Classification of regions of enrichment on the basis of differences between conditions. Changes in TSS-distal SWI/SNF binding upon SMARCB1 re-expression were evaluated at each RoE by dividing the library-size-normalized immunoprecipitation signal for SMARCC1 and SMARCA4 in the doxycycline condition by that in the no-doxycycline condition. If the geometric mean of change was greater than 1.5-fold and both factors showed increased signal,

the RoE was called as 'gained/strengthened'. In reverse, if the geometric mean of change was less than 2/3-fold and both factors showed decreased signal, the RoE was called as 'lost/weakened'. Other sites were called as 'unchanged'. Sites that were called in the no-doxycycline condition and sites where the average SMARCA4 + SMARCC1 signal in the no-doxycycline condition was more than half the signal in the doxycycline condition were considered as SWI/SNF binding sites in the no-doxycycline condition (used in **Fig. 3a**, left). Complementary selection was performed for SWI/SNF binding sites in the doxycycline condition (used in **Fig. 3a**, right).

ChIP-seq visualization. Genomic profiles for visualization were generated using Gaussian smoothing with $\sigma = 100$ bp after library size normalization (for example, in **Fig. 3c,d** or output wig files). The heat maps in **Figure 4c** were centered on the position with the highest signal in the smoothed profile obtained by summing the four tracks considered (no doxycycline SMARCC1, no doxycycline SMARCA4, doxycycline SMARCC1, and doxycycline SMARCA4). The heat maps show input-subtracted values, whereas the browser shots show raw smoothed signal. The average profiles for each class in **Figure 3c** (for example, stable) were obtained as the 0.1–0.9 trimmed linear mean at each position. The scatterplots in **Figures 3b** and **4b** were obtained as (total immunoprecipitation signal in the RoE per million mapped reads + pseudocount of 0.1)/(matching input + 0.1).

Identification of super-enhancers. Super-enhancers were identified with an approach slightly modified from the original method¹⁶. H3K27ac RoEs were called as described above. We did not remove TSS-proximal peaks but stitched all RoEs within 12.5 kb. For each stitched RoE, instead of removing false positives from stitched enhancer peaks that encompassed active TSSs, we calculated immunoprecipitation and input signals only in portions that did not intersect with H3K4me3 RoEs. This approach excludes the high H3K27ac signal found at active promoters while still allowing enhancers on either side of a promoter to be stitched. Each super-enhancer was associated with the closest active TSS, as defined above, within 300 kb. If more than one gene was similarly close to a super-enhancer (at most 50 kb further away than the closest gene), the additional genes were also included on the list of super-enhancer-associated genes.

Gene ontology analysis of enhancers with increased SWI/SNF binding. GO analysis for SMARCB1-dependent SWI/SNF enhancers was performed as follows. GO databases were downloaded from <http://geneontology.org/> on 29 April 2014. Each enhancer was associated with the closest active TSS within 100 kb and within conserved topology-associated domains. P values for gene set enrichment for genes associated with enhancers overlapping a gained/strengthened SWI/SNF RoE were calculated relative to genes associated with any enhancer using hypergeometric tests. q values were obtained on the basis of the Benjamini–Hochberg procedure. The top five terms and selected developmental terms are displayed in the figures.

RNA-seq processing. Initial processing. The sequenced reads from each sample were aligned to the human genome + transcriptome assembly GRCh37.72 using TopHat (v2.0.8)³⁷ with default parameters except that novel junction search was turned off (`-G <gtf> --no-novel-juncs`). The transcriptome was self-merged to allow processing with the Cufflinks v2.1.1 tool `cuffdiff`³⁸, `'cuffcompare -s hg19.fa -CG -r GRCh37.72.gtf GRCh37.72.gtf'`. Different conditions for a given cell line were compared using `cuffdiff` with default parameters and bias correction (`-G <gtf> -b options`).

Relating RNA-seq changes to ChIP-seq changes. Each SWI/SNF or H3K27ac RoE was associated with the closest active TSS, as defined above. The connection between change in ChIP-seq signal and change in RNA-seq signal was studied for TSS-proximal and TSS-distal RoEs separately. Only RoEs for which the closest active TSS was between 5 kb and 100 kb away were retained for the TSS-distal analysis. Change in immunoprecipitation signal was quantified as the total immunoprecipitation signal in the RoE per million mapped reads + a pseudocount of 0.1. Change in RNA signal was quantified as the normalized gene-level count value from `cuffdiff` + 5. The ratio of the immunoprecipitation signal for the doxycycline sample divided by that for the no-doxycycline sample was used to categorize RoEs into four groups: RoEs with more than 3-fold signal gain, RoEs with between 1.5- and 3-fold signal gain, RoEs with less than 1.5-fold signal change, and RoEs with more than 1.5-fold signal loss. The ratio of RNA-seq signal for the doxycycline sample divided by that for the no-doxycycline sample was plotted for each category.

Gene set enrichment analysis. GSEA³⁹ was performed on the basis of *P* values for gene expression changes output by Cufflinks. The weights were set as $-\log(P)$ for upregulated genes and $\log(P)$ for downregulated genes. gsea2-2.0.13.jar was run with recommended parameters.

Clustering of genes and gene ontology analysis. The heat map for RNA-seq results in **Supplementary Figure 6** shows \log_2 (fold change) values for 2,171 genes, where replicate experiment sets were considered separately. The fold change values were calculated as the normalized gene-level count value from cuffdiff + 5 for the doxycycline sample divided by that for the no-doxycycline sample. Genes were selected on the basis of two requirements: (i) more than a two-fold change in at least two of the sample pairs and (ii) more than 50 normalized reads mapping to the gene in at least two of the samples. The samples were subjected to *k*-means clustering with ten clusters using the R function heatmap with the Pearson correlation between samples ($1 - r$) as the distance metric. GO analysis was performed for each cluster separately as follows. GO databases were downloaded from <http://geneontology.org/> on 20 April 2014. All genes for which more than 50 normalized reads mapped to the gene in at least two of the samples were used as background. *P* values for enrichment were calculated using hypergeometric tests. *q* values were obtained on the basis of the Benjamini–Hochberg procedure. Selected GO terms are displayed in the figure, including any term with $q < 1 \times 10^{-4}$ and developmental terms with $q < 1 \times 10^{-2}$.

Statistical analysis. All *in vitro* experiments were performed in triplicate (cell culture) unless specifically stated in the figure legends, with means and standard deviation reported. *P* < 0.05 was considered significant. **P* < 0.05,

***P* < 0.001, unless specifically stated in the figures or figure legends. All GO enrichment analyses were performed using hypergeometric tests and were corrected for multiple tests using the Benjamini–Hochberg method (R functions phyper(lower.tail = F) and p.adjust(method = “BH”). Comparison of changes in gene expression for genes near the different enhancer classes was performed using two-sided *t* tests (R function t.test). Exact *P* values and *q* (FDR) values are reported for both.

31. Helming, K.C. *et al.* ARID1B is a specific vulnerability in ARID1A-mutant cancers. *Nat. Med.* **20**, 251–254 (2014).
32. Staahl, B.T. *et al.* Kinetic analysis of npBAF to nBAF switching reveals exchange of SS18 with CREST and integration with neural developmental pathways. *J. Neurosci.* **33**, 10348–10361 (2013).
33. Langmead, B., Trapnell, C., Pop, M. & Salzberg, S.L. Ultrafast and memory-efficient alignment of short DNA sequences to the human genome. *Genome Biol.* **10**, R25 (2009).
34. Kharchenko, P.V., Tolstorukov, M.Y. & Park, P.J. Design and analysis of ChIP-seq experiments for DNA-binding proteins. *Nat. Biotechnol.* **26**, 1351–1359 (2008).
35. de Hoon, M.J.L., Imoto, S., Nolan, J. & Miyano, S. Open source clustering software. *Bioinformatics* **20**, 1453–1454 (2004).
36. Saldanha, A.J. Java Treeview—extensible visualization of microarray data. *Bioinformatics* **20**, 3246–3248 (2004).
37. Kim, D. *et al.* TopHat2: accurate alignment of transcriptomes in the presence of insertions, deletions and gene fusions. *Genome Biol.* **14**, R36 (2013).
38. Trapnell, C. *et al.* Differential analysis of gene regulation at transcript resolution with RNA-seq. *Nat. Biotechnol.* **31**, 46–53 (2013).
39. Subramanian, A. *et al.* Gene set enrichment analysis: a knowledge-based approach for interpreting genome-wide expression profiles. *Proc. Natl. Acad. Sci. USA* **102**, 15545–15550 (2005).